POLISH MARITIME RESEARCH 4 (128) 2025 Vol. 32; pp. 59-77
10.2478/pomr-2025-0050

Drag Reduction and EEXI Compliance: Evaluating Air Lubrication for In-Service Ships via CFD

Nawar Abbas*
Latakia University, Department of Maritime Engineering, Latakia, Syrian Arab Republic
Rami Hawa
Prof. Latakia University, Department of Maritime Engineering, Latakia, Syria, Syrian Arab Republic
Wehad Hatem
PhD. Student, Latakia University Department of Maritime Engineering, Latakia, Syria, Syrian Arab Republic

* Corresponding author: *noarabbas@yahoo.com; dr.nawarnabilabbas@latakia-univ.edu.sy (Nawar Abbas)*

ABSTRACT

This research used CFD techniques to study the effect of air lubrication technology on the Energy Efficiency Existing Ship Index (EEXI), developed by the International Maritime Organization. The Unsteady RANS (Reynolds-Averaged Navier-Stokes Equation) and the k-ω SST turbulence model were used to solve the Navier-Stokes equations governing flows, while the Volume of Fluid (VOF) method was used to solve the two-phase (air-water) flow. The JBC bulk carrier was chosen for this study because its shape closely resembles that of bulk carriers and tankers currently operating in the merchant fleet. Initially, the ship model was studied alone, without any appendages, at a scale of 1:40. The MP687 propeller was used with this ship in a self-propulsion test. An Open Water Test was conducted, with the Verification and Validation procedure being applied to the CFD results obtained for the JBC alone, in order to verify the accuracy of the numerical grid and the equations and turbulence models used to complete these calculations. The wave effect and ship motions (pitch, heave, roll, etc.) were neglected and the calculations were carried out in calm water. Then, air flow directing strakes were added to the bottom of the parallel body of the ship to investigate the impact of air lubrication on the EEXI value. At this stage, air lubrication was used for the ship alone, without a propeller, and then again for the ship with a propeller. Several types of air flow-directing strakes were tested, to trap air beneath the parallel body of the hull. The implementation of air lubrication technology with the proposed strakes reduced total ship resistance, resulting in a 16.67% improvement in the attained EEXI value. This reduction directly correlates with lower CO_2 emissions per unit of transport work (measured in grams of CO_2 per ton × nautical mile), demonstrating the system's potential to enhance compliance with IMO's carbon intensity regulations, without compromising operational performance.

Keywords: Energy Efficiency Existing Ship Index, JBC, CFD, URANS, MP687, Air Injection, Drag Reduction

INTRODUCTION

The shipping industry, which serves as the backbone of international trade, is facing increasing pressure to minimise its environmental impact. International maritime policies, predominantly spearheaded by the International Maritime Organization (IMO), include stringent regulations on ship energy efficiency and GHG emissions abatement. The most important of these are the Energy Efficiency Design Index (EEDI) for new Ships (constructed on or after 01.01.2013), the Energy Efficiency Existing Ship Index EEXI for Existing ships (constructed before 01.01.2013), and the Ship Energy Efficiency Management Plan (SEEMP) for all ships, supplemented by the recently introduced Carbon Intensity Indicator (CII) rating system, there is a continuous effort to improve their values for both new ships and ships in service [1–3]. Although these regulations provide a necessary foundation, effective enforcement and the widespread adoption of cutting-edge technologies are more critical to achieving the IMO's ambitious decarbonisation targets [4–6]. Air lubrication, an emerging and fast-developing technology that reduces hydrodynamic drag through the creation of a carpet of air bubbles beneath the hull of a ship, presents a powerful option for drastically increasing fuel efficiency and facilitating compliance with these evolving standards. This article discusses how air lubrication systems (ALS) can serve as good ways to complement IMO's energy efficiency standards compliance, by reviewing their operational principles, established benefits, and regulatory framework [7–9].

The concept of reducing ship resistance through air injection has been considered by designers for decades but recent technological advances have placed air lubrication at the forefront of the green shipping revolution. Early research was, primarily, theoretical and laboratory-oriented but established the underlying concepts for air layer drag reduction [10]. McCormick and Bhattacharyya (1973) undertook early studies of microbubble drag reduction, establishing the theoretical basis for subsequent research. Their studies demonstrated the potential for a large amount of friction reduction through the injection of air. More detailed experimental studies on flat plates were conducted by Madavan et al. (1984; 1985), which further established the drag reduction capability of air bubbles in turbulent boundary layers. These publications were significant in bringing the concept from being a theory to the level of being considered for practical implementation [11].

The Air Lubrication System (ALS) in a ship operates by blowing air bubbles between a ship's hull and the water, effectively cutting down the skin friction that ships normally experience during cruising (Mäkiharju et al., 2012) [12]. The technique significantly reduces drag, thus enhancing fuel efficiency and general ship performance [12, 13]. Among its greatest benefits are the reduction of fuel oil consumption (FOC) and greenhouse gas emissions, as well as long-term operational expenses [12]. These advantages, however, come at the expense of significant initial investment, continual maintenance of the system, and potential inefficiencies during harsh seas.

For example, Mitsubishi Heavy Industries Ltd (MHI) brought forth the Mitsubishi Air Lubrication System (MALS) as a means of lowering resistance using air lubrication [14]. Initially deployed on the Yamatai cargo ship, MALS was then utilised on other ship types, container ships, and cruise ships, following intensive CFD simulations and model testing to verify its performance. The MALS has been proven to have a fuel saving of approximately 5% and a CO_2 emissions reduction of 6%. When utilised on Aida Prima and Aida Perla cruise ships, the predicted fuel savings reached 7% [14–16]. Samsung Heavy Industries also studied air resistance reduction through air layer generation on a 66,000 DWT bulk carrier [17]. Their research employed precise airflow control with injector plenum units that led to stable air layers and 8–10% drag reduction, as well as 7–9% power consumption reductions. London's Silverstream Technologies unveiled a versatile ALS aimed at cost savings and environmental gains [18–20]. Its system employs fine, continuous bubble streams, optimised for hull coverage, with demonstrated fuel savings of 4–10% and additional benefits such as lower propeller noise and hull fouling.

Other innovators also include Armada Technologies, which developed a Passive Air Lubrication System (PALS) that is compressor-free and uses the ship's motion to generate a smooth air-water mixture [21]. Alfa Laval's OceanGlide solution achieves up to 12% gains in propulsion efficiency [22].

While the benefits have been demonstrated, the extensive implementation of ALS has been slowed down by pragmatic concerns. Industry preference is for testing ALS on newbuild ships rather than retrofitting existing ships, mainly because performance estimates during sea trials may not reflect the full range of operations. Therefore, ALS efficiency validation using wide real-world operating data is important, especially as accurate data is needed to derive a ship's CII rating. Empirical evidence continues to be paramount for valid ALS performance evaluation.

The remainder of this paper is organised as follows: the second section briefly reviews the numerical method implemented in this work. In the third section, the authors validate the numerical method using JBC and MP687 propeller test cases. Next, the geometry of the proposed strakes, as well as the configuration and numerical environment, are described. A summary of the results is demonstrated in the final section.

MATERIALS AND METHODS

GOVERNING EQUATIONS

To address the problem, both the Navier-Stokes equations and the continuity equation were employed. When turbulence is modelled using the Reynolds averaging approach, the Navier-Stokes equations are reformulated using Cartesian tensor notation in the following manner:

$$\frac{\partial \rho}{\partial t} + \frac{\partial(\rho u_i)}{\partial x_i} = 0 \quad (1)$$

$$\frac{\partial(\rho u_i)}{\partial t} + \frac{\partial}{\partial x_j}\left(\rho u_i u_j\right) = \frac{\partial \bar{p}}{\partial x_j} + \frac{\partial}{\partial x_j}\mu\left(\frac{\partial u_i}{\partial x_j} - \rho\overline{u_i' u_j'}\right) + S_j \quad (2)$$

where u_i and u_j denote the time-averaged values (i, j = 1, 2, 3) of the velocity component; p is the time-averaged value of the pressure; ρ is the fluid density; μ is the dynamic viscosity coefficient; $\rho\overline{u_i' u_j'}$ is the Reynolds stress term; and S_j is the source term.

TURBULENCE MODEL AND TREATMENT OF FREE SURFACE

To simulate the Reynolds stress term, the k-ω SST turbulence model of Menter [23] was employed. The model was selected since it is superior to the baseline k-ω and k-ε models, particularly when accurately simulating viscous flow fields. It is commonly employed in ocean engineering, along with the URANS approach, due to its ability to produce results which are very similar to experimental results [24–28].

To solve the free surface, Hirt and Nichols' Volume of Fluid (VOF) method [29] was used; this tool is widely employed in commercial CFD software. VOF is focused on the propagation of the interface between two immiscible fluids and is suitably positioned to handle free surface flows. It is favoured because it is computationally inexpensive (in terms of memory), it is easy to code, and it is able to adequately track liquid interfaces [30]. Its accuracy has been validated in numerous studies relating to marine free surface flows [28, 31–33], justifying its use for the current case.

GEOMETRY AND THE NUMERICAL ENVIRONMENT

A scaled double model of a Japan Bulk Carrier (JBC) was selected for this study, at a scale of 1:40, due to its widespread use as a benchmark for CFD validation in the shipbuilding field [34, 35]. Fig. 1 illustrates the geometry of the JBC ship. The dimensions of the model were 7.000 m in length, 1.125 m in breadth, and with a draught of 0.4125 m and a block coefficient of 0.8580. CFD was conducted at a steady velocity of 1.179 m/s, yielding a Reynolds number of 7.46×10^6. The relatively low Froude number of 0.142 indicated that the effects of water surface deformation could be reasonably ignored.

Fig. 1. JBC geometry [36]

The propeller used was an MP687, which has a five-bladed propeller; the main specifications are detailed in Table 1 and its geometric configuration is depicted in Fig. 1 and Fig. 2. According to the data presented in the table, the propeller has a diameter of 203 mm. Open water test results for the MP687 model were made available during the Tokyo Conference held in 2015, as reported in [37].

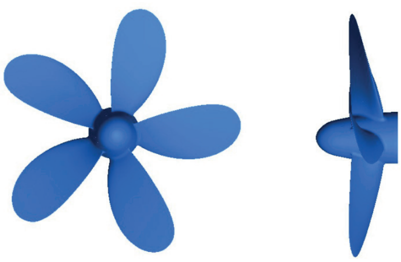

Fig. 2. The MP687 propeller

Tab. 1. Propeller MP687 parameters [37]

Diameter	[m]	0.203
Pitch ratio, r/R = 0.7	[-]	0.75
Expanded area ratio	[-]	0.5
Angle of rake	[°]	5
Number of blades	[-]	5
Sense of rotation	[-]	Clockwise

To study the influence of the numerical mesh on the CFD results, Ansys ICEM was used to create three different mesh configurations for the bare hull analysis of the JBC ship model. These meshes (called G3, G2, and G1) had approximately 1.80 million, 3.11 million, and 5.40 million cells, respectively. The mesh refinement was mainly focused on the boundary layer area near the hull surface (Fig. 3a). The coarsest mesh was the starting point and the finer grids were created by successively refining this mesh, by multiplying the number of cells in each spatial direction (x, y, z) by a factor of 1.2. In all meshes, the initial node was placed away from the wall, where $y^+ > 30$ so that wall functions were applied throughout the simulations.

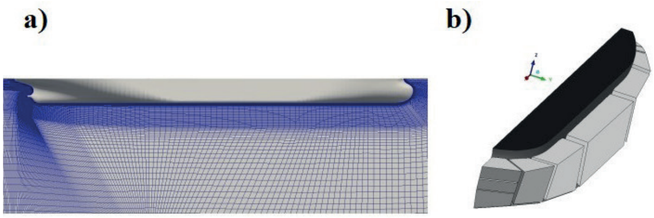

Fig. 3. a) Computational grid of JBC, b) Blocks of the boundary layer

For the open water testing of the MP687 propeller, the mesh domain was divided into the static and rotating areas. Fig. 4 shows the mesh pattern in the stator (static) and rotor (rotating) zones. The static part of the mesh was meshed with Ansys ICEM; whereas, the rotating domain was meshed by using a combination of ICEM and snappyHexMesh utilities.

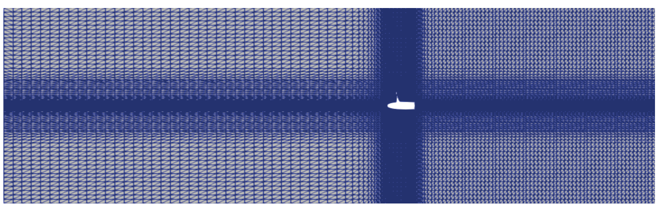

Fig. 4. Computational grid in the symmetry plane

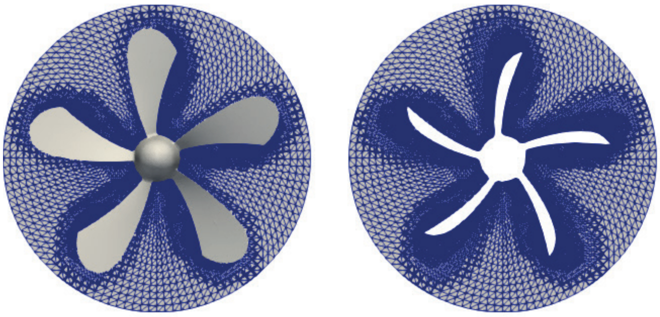

Fig. 5. Computational grid in the boundary layer near to the propeller

Three mesh densities were used to calculate the propeller performance, with approximately 1.5, 2.6, and 4.5 million cells. Refinements were also localised close to the boundary layer on the surface of the propeller (refer to Fig. 5). Like the hull mesh, the medium and fine meshes were achieved through successively refining the coarse mesh. This was achieved by equally increasing the cell number in each spatial direction (x, y, z) by a factor of 1.2 in the entire domain. In each mesh, the initial grid point was positioned, as recommended in ITTC 2011 [38] and ITTC 2014 [39], such that $y^+ > 30$ relative to the wall; this allowed wall functions to be used throughout the calculations. A 1.2 expantion ratio was used and this is the proposed value from ITTC 2014 [39].

Pressure-velocity coupling, and the solution process in general, were controlled by the coupled algorithm. Spatial discretisation parameters for the convection terms of the governing equations are provided in Table 2.

Tab. 2. The numerical settings of the spatial discretisation of the convection terms

Gradient	Pressure	Momentum	Volume Fraction	Turbulent Kinetic energy	Specific Dissipation Rate
Least Squares Cell--Based	PRESTO	Second Order Upwind	Compressive	Second Order Upwind	Second Order Upwind

Table 3 illustrates the detailed numerical simulation parameters used in ANSYS-Fluent. To properly control the time step, the procedure was carried out according to ITTC recommendations. The maximum CFL number was set to 1 and, with this value, the largest time step used was 0.0005 seconds, as shown in Table 3. The smallest time-step recommended by the ITTC 2011 [38] and ITTC 2014 [39] is $0.001\ \frac{L}{U}$, which, in our case, corresponds to 0.006. However, in our study the maximum time step was 0.0005, meaning that the time step size is sufficiently small to correctly resolve the flow.

Since the propeller was analysed, and according to ITTC recommendations [38], [39], each revolution of the propeller must be completed within 180 time-steps. In our study, the propeller rotation speed was 10 rps, which meant that one revolution took 0.1 seconds. With the chosen time step of 0.0005, the number of time steps required to complete one revolution of the propeller was 200, which fully complies with the ITTC requirements.

Tab. 3. Detailed numerical simulation parameters

(a) Solver		**(b) VOF Model**		**(c) Boundary Conditions**	
Type	Pressure based	**Homogeneous Models**	Volume Of Fluid	**Bottom, Sides, Ship, and Strakes**	No-slip wall
Velocity formulation	Absolute	**Volume Fraction Parameters**	Formulation-Implicit	**Inlet**	Velocity inlet Velocity Specification Method-Magnitude, normal to Boundary Velocity Magnitude 1.179 m/s Phase-water Volume fraction 1.0
Time	Transient	**Volume Fraction Cutoff**	1e-06	**Injector**	Velocity inlet Velocity Specification Method-Components Coordinate System-Cartesian (X, Y, Z) X-Velocity [m/s] -1.0 X-Velocity [m/s] 0 X-Velocity [m/s] 0 Phase-water Volume fraction 0
Simulation time	100 [s]	**Courant number**	0.25	**Outlet**	Pressure Outlet
Time step size	0.0005 [s]	**Interface modelling-type**	Sharp	**Top**	Symmetry
Number of time steps	200000	**Body force formulation**	Implicit Body Force	**Interface between rotor and stator**	Interface

(a) Solver		(b) VOF Model		(c) Boundary Conditions	
Maximum iterations	10	**Air-primary phase**	Phase material – air	**Propeller**	Wall-Moving Wall Motion: Relative to the Adjacent Cell Zone Components-Velocity Components X-Velocity [m/s] 0 Y-Velocity [m/s] 0 Z-Velocity [m/s] 0
Convergence Target Residual	0.00001	**Water – secondary phase**	Phase material – water-liquid	(d) Mesh Interfaces	
Gravity	ON Value on Z [m/s^2] -9.81	**Phase Interaction**	Air Water	**Interfaces**	Select the interface surfaces
				Interface Name Prefix	Interface→Create
Multiphase	Mixture model VOF	**Surface Tension Coefficient (N/m)**	Constant-0.073	(e) Cell Zone Conditions (Rotor Zone, Propeller Zone)	
Fluids	Air and Water	**Global Options**	Surface tension force modelling	**Zone function**	Mesh Motion
		Turbulence Model	Shear Stress Transport (SST)	**Mesh Motion details**	Relative Specification-Relative To Cell Zone-absolut UDF-Zone Motion Function-none Rotation Axis Origin X[m] 0.0915426 Y[m] 0 Z[m] 0.129549 Rotation Axis Direction- X-1 Rotational Velocity-Speed[rev/min] 600

ENERGY EFFICIENCY EXISTING SHIP INDEX (EEXI)

The Energy Efficiency Existing Ship Index (EEXI) is a regulatory standard, established by the International Maritime Organization (IMO) to comply with energy efficiency requirements aimed at reducing carbon dioxide (CO_2) emissions. This standard comprises two key values: $EEXI_{required}$ and $EEXI_{attained}$, both of which must satisfy the following criterion [40], [41]:

$$EEXI_{\,attained} \leq EEXI_{required} \tag{3}$$

$EEXI_{required}$ is calculated according to [42]:

$$EEXI_{required} = \left(1 - \frac{Y}{100}\right) a \times b^{-c} \tag{3}$$

Whereas Y, a, b, and c are tabulated values stated in the resolution established by the IMO Marine Environment Protection Committee [42], [43], $EEXI_{\,attained}$ is calculated according to [40], as follows:

$$\mathbf{EEXI_{att}} = \frac{\left(\prod_{j=1}^{n} f_j\right)\left(\sum_{i=1}^{nME} P_{ME(i)} . C_{FME(i)} . SFC_{ME(i)}\right) + \left(P_{AE} . C_{FAE} . SFC_{AE}\right) + \left(\left(\prod_{j=1}^{n} f_j . \sum_{i=1}^{nPTI} P_{PTI(i)}\right) C_{FAE} . SFC_{AE}\right) - \left(\sum_{i=1}^{neff} f_{eff(i)} . P_{eff(i)} C_{eff(i)} SFC_{ME}\right)}{f_i . f_c . f_l . Capacity . f_w . V_{ref} . f_m} \tag{4}$$

Where:

$P_{ME(i)}$: 75% of the Maximum Continuous Rating (MCR) of the main engine;

$C_{FM(i)}$: CO_2 emission factor of the fuel used in the main engine;

$SFC_{ME(i)}$: Specific fuel consumption of the main engine at a power equal to $P_{ME(i)}$;

$P_{AE(i)}$: A fraction of the main engine power, given by the following relation [41]:

$$\left(0.05 \times \left(\sum_{i=1}^{nME} MCR_{ME(i)} + \frac{\sum_{i=1}^{nPTI} P_{PTI(i)}}{0.75}\right)\right) \tag{5}$$

$P_{PTI(i)}$ is the power of the shaft motor. If it is not present, its value is set to zero and the equation becomes:

$$P_{AE} = \left(0.05 \times \left(\sum_{i=1}^{nME} MCR_{ME(i)}\right)\right) \tag{6}$$

Where:

$C_{AE(i)}$: CO_2 emission factor of the fuel used in the auxiliary engine, stated as [41];

$SFC_{AE(i)}$: Specific fuel consumption of the auxiliary engine at a power equal to 50% of the MCR_{AE};
Capacity: Ship capacity, which represents the deadweight for bulk carriers and oil tankers;
f_j: Ship-specific design elements;
P_{PTI}: Power of the Shaft motor;
P_{eff}: Innovative mechanical energy-efficient technology for the main engine;
f_{eff}: Factor of each innovative energy efficiency technology;
C_{eff}: Correction factor for innovative energy efficiency technology;
f_l: Capacity factor for technical/regulatory limitation on capacity;
f_i: Capacity correction factor for ice-class ships;
f_c: Cubic capacity correction factor;
Capacity: for bulk carriers, tankers, gas carriers, LNG carriers, ro-ro cargo ships (vehicle carriers), ro-ro cargo ships, ro-ro passenger ships, general cargo ships, refrigerated cargo carriers and combination carriers, this is the deadweight of the intended ship; whereas, the capacity for passenger ships and cruise passenger ships is the gross tonnage;
V_{ref}: Ship speed at P_{ME};
f_w; Factor for speed reduction at sea.

In this study, the ships studied were bulk carrier ships, with no innovative energy efficiency technology equipped to the Main Engine and no shaft generator or shaft motor installed. Therefore, Eq.)4(can be simplified as follows:

$$\mathbf{EEXI_{attained}} = \frac{(0.75\, MCR_{ME(i)} \times C_{FME(i)} \times SFC_{ME(i)}) + (0.05 \times MCR_{ME(i)} \times C_{FAE} \times SFC_{AE})}{Capacity \times V_{ref}} \quad)7($$

Also, Eq. (7) (where $\boldsymbol{MCR_{ME(i)} = const}$) can be simplified as follows:

$$\mathbf{EEXI_{attained}} = \frac{MCR_{ME(i)}\left((0.75 \times C_{FME(i)} \times SFC_{ME(i)}) + (0.05 \times C_{FAE} \times SFC_{AE})\right)}{Capacity \times V_{ref}} \quad)8($$

VERIFICATION AND VALIDATION (V&V)

A validation and verification (V&V) analysis was performed, as illustrated in Fig. 6, by following the procedures outlined by Stern et al. (2001) [44 – 47], the International Towing Tank Conference (ITTC, 2008) [48], and the method outlined by Xing and Stern (2010) [49].

The verification procedure (see Fig. 7) involves a detailed evaluation of the numerical uncertainty U_{SN} in the simulation, along with an analysis of the direction and size of the associated numerical error δ^*_{SN} , where:

$$U_{SN}^2 = U_I^2 + U_T^2 + U_G^2 \quad)9($$

In Eq. (10):
U_I is the iterative uncertainty and is equal to half the range between the maximum S_U and minimum S_L solution values for the oscillatory iterative convergence condition $U_I = \left|\frac{1}{2}(S_U - S_L)\right|$;
U_T is the time-step uncertainty. U_T was not evaluated in this study due to a constant Courant–Friedrichs–Lewy number (CFL number) [50], [51]. In this study, the maximum CFL number was set to 1;
U_G is the grid uncertainty.

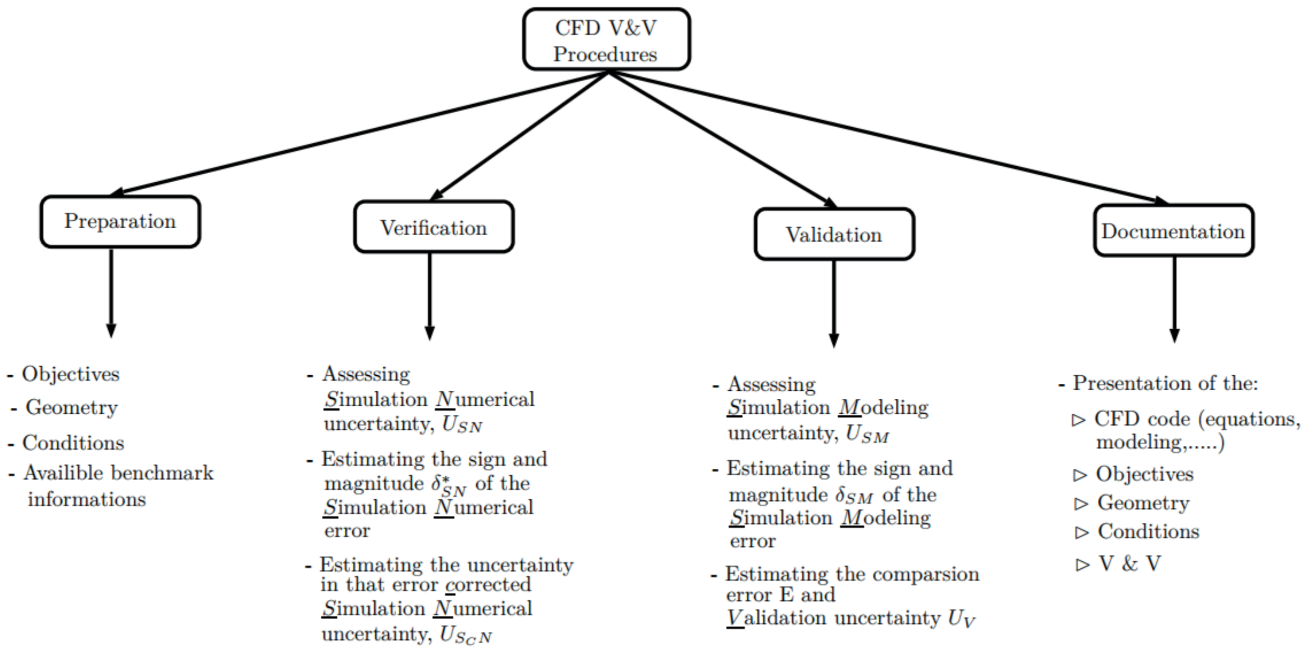

Fig. 6. Verification and Validation procedure according to ITTC 2008 [48]

S_1, S_2 and S_3 are the simulation results of the fine, medium, and coarse grids, respectively. r_k is the grid refinement ratio of the k^{th} input parameter necessary to conduct a grid convergence study. This ratio indicates the proportion between the dimensions of the coarse and fine mesh cells; it can be readily determined in the case of a structured grid. In this work, since only a structured mesh was utilised, the grid refinement ratio was assumed to be $r_k = \frac{\Delta x_2}{\Delta x_3} = \frac{\Delta x_1}{\Delta x_2}$ [48], where $\Delta x_{1,2,3}$ refers to the spacing of the fine, medium, and coarse grids.

R_i is the convergence ratio, which is equal to $R_i = \left|\frac{S_2 - S_1}{S_3 - S_2}\right|$.

The estimated error δ_G^* and order of accuracy P_G were calculated as:

$$\delta_{RE_k}^* = \frac{S_2 - S_1}{r_G^{P_k} - 1} \tag{10}$$

$$P_k = \frac{\ln((S_3 - S_2)/(S_2 - S_1))}{\ln(r_k)} \tag{11}$$

where r_k is the refinement ratio (1.2 in the present work).

Additionally, ITTC (2008) also noted the usefulness of a multiplicative correction factor as a quantitative approach. It is useful for assessing how near solutions are to the asymptotic range, assessing the effect of the higher-order terms, and estimating error levels and uncertainty limits. The error is defined as $\delta_k^* = C_k \times \delta_{RE_k}^*$, where C_k is the correction factor and is defined as:

$$C_k = \frac{r_k^{P_k} - 1}{r_k^{P_{k_{est}}} - 1} \tag{12}$$

$P_{k_{est}}$ is the limiting order of accuracy of the first term as the spacing size approaches zero and $C_k \to 1$.

The grid uncertainty was calculated using:

$$\begin{aligned} U_k &= (|C_k| + |1 - C_k|)\left|\delta_{RE_k}^*\right|, \quad C_k \geq 1 \\ U_k &= (2|1 - C_k| + 1)\left|\delta_{RE_k}^*\right|, \quad C_k < 1 \end{aligned} \tag{13}$$

If solutions are near to the asymptotic range, C_k becomes close to 1 and δ_k^* is calculated as $\delta_k^* = C_k \times \delta_{RE_k}^*$ while U_{kC} is estimated using $U_{k_C} = |1 - C_k|\left|\delta_{RE_k}^*\right|$, which has the correct form for both $C_k < 1$ and $C_k > 1$.

Validation includes a comparison of the simulation's modelling uncertainty U_{SM} with reference to experimental data D. It also includes an estimate of the direction and magnitude of the modelling error δ_{SM} if the conditions are good.

Comparison error E is defined as the discrepancy between experimental data D and the simulation results S. Validation is deemed to have been successful at the validation uncertainty level U_V if the size of the comparison error E is less than U_V, where $(U_V^2 = U_D^2 + U_{SN}^2)$ and U_D is the experimental measurement uncertainty.

The verification and validation parameters of the JBC calculations are shown in Table 4 and Table 5. Table 4 compares the C_T from the experiment [52] with the numerical results from the three grids when Fr = 0.142. The table shows that the maximal value of the error is 6.52% with the coarse grid but decreases to 2.10% in the fine grid.

Table 5 demonstrates the verification parameters, which show a monotonic convergence ($0 < R_G < 1$), the error estimate δ_G^* is smaller than 4%S_1, the value of U_G%S_1 is equal to 5.24, and Iterative Uncertainty for the calculations is very small, so it can be considered as negligible. The value of the data uncertainty U_D%D was set to 1, as per the recommendations of the Tokyo conference [53]. As shown in Table 5, the simulated numerical uncertainty U_{SN} and validation uncertainty U_V are smaller than 5.5%S1.

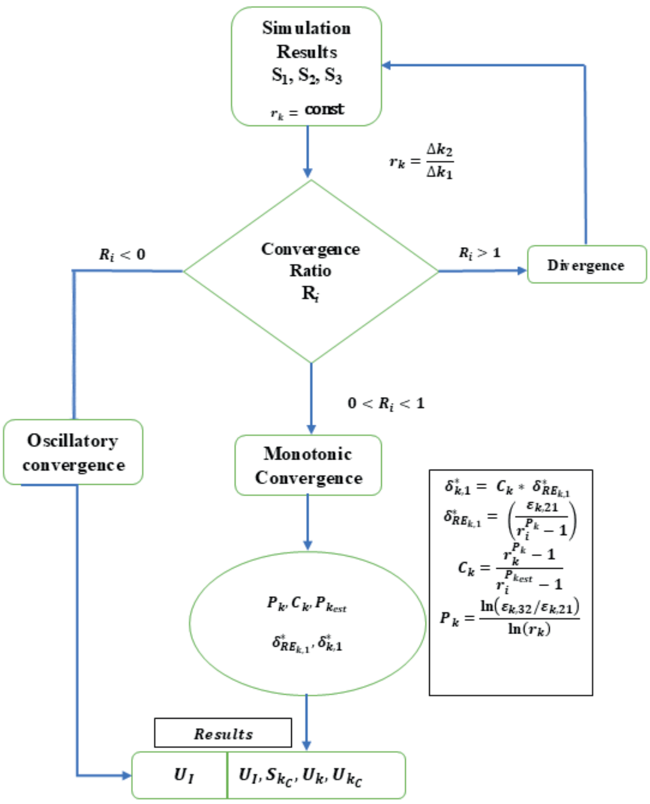

Fig. 7. Verification procedure [44], [48]

Tab. 4. Numerical results of the total resistance coefficient of the JBC from different grids

Grid	Cell number × 10⁶	$C_T \times 10^6$	Error (%)
Exp	-	4.289	-
Coarse	1.80	4.010	6.52
Medium	3.11	4.130	3.73
Fine	5.40	4.200	2.10

Tab. 5. V&V of the total resistance coefficient of the JBC

Parameter	R_G	P_G	C_G	$U_G\%S_1$	$U^*_{GC}\%S_1$	$U_{GC}\%S_1$	S_C	$U_D\%D$	$U_{SN}\%S_1$	$U_V\%S_1$
C_T	0.58	2.95	1.62	5.24	3.78	1.45	4.298	1	5.24	5.33

According to the results shown above, a slight difference exists between the CFD results obtained in this study and the experimental results. However, there is a satisfactory agreement in the resistance value between both sets of results, indicating that the test and simulation performed in this study can yield accurate values of the forces affecting the JBC ship.

The V&V procedure was conducted on the numerical results of the forces and moments affecting the MP687 propeller. The results of the open water testing of the model MP687 propeller were published at the Tokyo Conference in 2015 [37].

The V&V procedure was applied to three parameters: thrust coefficient K_T, torque coefficient K_Q, and propeller efficiency η_0, at the advance ratios of J=0.2 (Table 6 and Table 7) and J=0.7 (Table 8 and Table 9). The value of the data uncertainty $U_D\%D$ was set to 1, in accordance with the recommendations of the Tokyo conference [53].

All of the results show monotonic convergence; the grid, simulation, numerical, and validation uncertainties for $K_T K_Q$, and η_0 are smaller than 5.5%S_1. Moreover, the error estimate δ^*_G is smaller than 3.5%S_1.

Experimental and numerical results both follow the same trends of variation under different loading conditions. However, there is a small variation in force coefficients between the CFD predictions and experimental measurements. Despite this difference, the selected numerical mesh and settings are acceptable for evaluating the flow behaviour behind the rotating propeller.

Tab. 6. Hydrodynamic forces affecting the MP687 propeller at J = 0.2

Parameter	Exp	Coarse	Error%	Medium	Error%	Fine	Error%
K_T	0.2949	0.28	5.05	0.287	2.67	0.29	1.66
$10\ K_q$	0.35	0.33	5.71	0.34	2.85	0.345	1.43
η_0	0.2681	0.27	-0.7	0.2687	-0.18	0.2675	0.23

Tab. 7. Verification and Validation of the hydrodynamic forces affecting the MP687 propeller at J = 0.2

Parameter	R_G	P_G	C_G	$U_G\%S_1$	$\delta^*_G\%S_1$	$U_{GC}\%S_1$	S_C	$U_D\%D$	$U_{SN}\%S_1$	$U_V\%S_1$
K_T	0.43	4.65	3.03	3.92	-2.35	1.57	0.293	1	3.93	4.05
$10\ K_q$	0.50	3.80	2.27	5.14	-3.29	1.85	0.35	1	5.14	5.23
η_0	0.81	1.15	0.53	1.79	0.95	0.84	0.263	1	1.79	2.05

Tab. 8. Hydrodynamic forces affecting the MP687 propeller at J = 0.7

Parameter	Exp	Coarse	Error%	Medium	Error%	Fine	Error%
K_T	0.0867	0.082	5.42	0.084	3.11	0.085	1.69
$10\ K_q$	0.15	0.14	7.22	0.145	3.91	0.147	2.58
η_0	0.6401	0.6525	-1.94	0.6454	-0.828	0.6442	-0.64

Table 9. Verification and Validation of the hydrodynamic forces affecting the MP687 propeller at J = 0.7

Parameter	R_G	P_G	C_G	$U_G\%S_1$	$\delta^*_G\%S_1$	$U_{GC}\%S_1$	S_C	$U_D\%D$	$U_{SN}\%S_1$	$U_V\%S_1$
K_T	0.5	3.80	2.27	4.17	-2.67	1.49	0.086	1	4.17	4.28
$10\ K_q$	0.4	5.02	3.41	5.27	-3.09	2.18	0.148	1	5.27	5.37
η_0	0.17	9.76	11.21	0.81	0.42	0.38	0.643	1	0.81	1.28

In order to validate the VOF method, the computational domain was extended to the region above the ship to include both air and water, thereby enabling the calculation of the free surface between them. As in the previous cases, structured grids were used and additional refinement was applied in the free surface region, in accordance with the ITTC 2014 [39] recommendations. The mesh used is shown in Fig. 8.

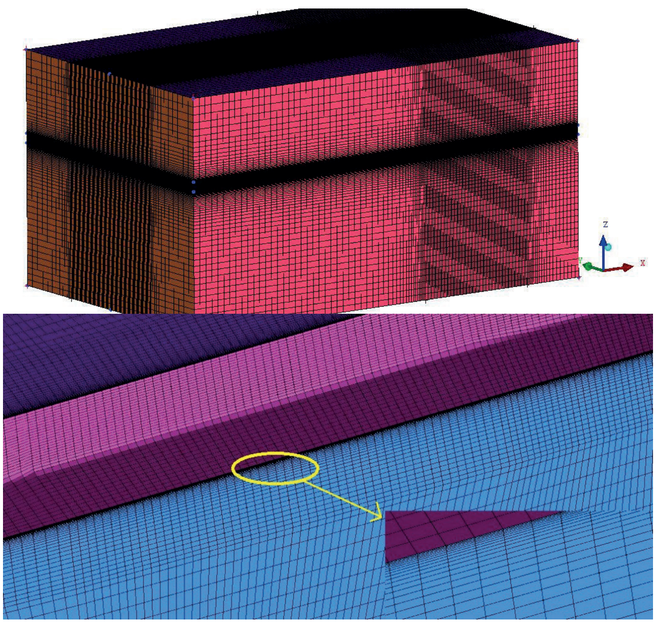

Fig. 8. Numerical grid for two-phase flow

Fig. 9 presents a comparison between the wave patterns obtained from the experimental results and those obtained from the numerical results. It can clearly be seen that the agreement between the two is good. Fig. 10 presents a direct comparison between the experimental result (EFD) and the numerical result (CFD) of the wave elevation along the entire ship hull. The available experimental results in this case are within the range $0 < \frac{X}{L_{PP}} < 0.9$. As can be seen from this figure, the agreement is reasonable.

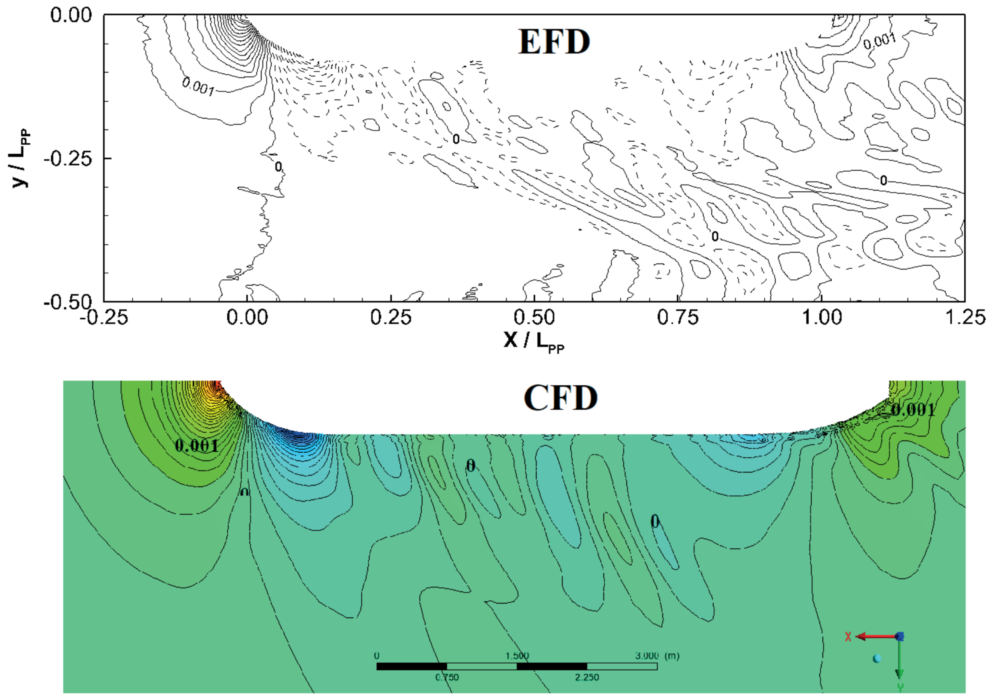

Fig. 9. Comparison between the wave patterns obtained from EFD and CFD

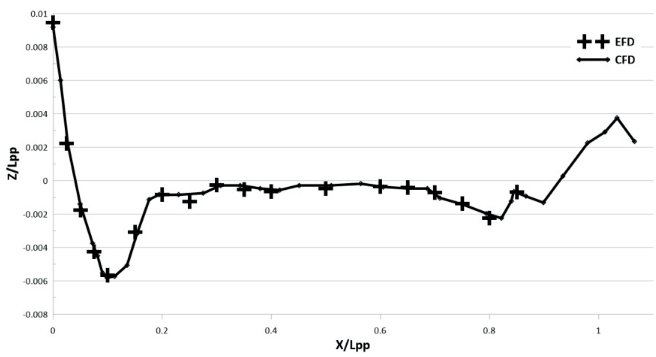

Fig. 10. EFD and CFD results of wave elevation along the entire ship hull within the range $0 < \frac{X}{L_{PP}} < 0.9$

AIR INJECTION UNDER THE JBC SHIP

In response to the growing risks associated with increased fossil fuel consumption, the International Maritime Organization (IMO) has developed an initial strategy to reduce Greenhouse Gas (GHG) emissions. This initial strategy serves as the cornerstone in the roadmap aimed at formulating a comprehensive IMO strategy to reduce GHG emissions from ships. The roadmap was adopted during the 70th session of the Marine Environment Protection Committee (MEPC), which decided to begin implementing the strategy in early 2023.

Maritime companies and stakeholders in the shipping industry quickly moved to develop various solutions aimed at improving energy efficiency in ships. These solutions range from replacing the ship's propeller with a more efficient one, using paints with relatively low friction coefficients, and limiting engine power through technologies that prevent it from exceeding a specific threshold.

Each of these approaches has notable drawbacks. More significantly, there is a risk that these measures may not be sufficient to meet the IMO's set standards. This will be put to the test during the first (annual, intermediate, or renewal) inspection for the International Air Pollution Prevention Certificate (IAPPC). If a ship fails to meet the required standards, the certificate will not be approved or renewed, preventing the vessel from operating internationally and potentially leading to its decommissioning and sale as scrap.

This highlights the significant challenge of complying with energy efficiency regulations, prompting the search for more effective and cost-efficient solutions. Among the most promising methods is air lubrication of the ship's hull, which has been recognised as an effective way to reduce the vessel's drag forces.

The objective of this study is to investigate the impact of applying air lubrication on reducing the total resistance of the bulk carrier JBC. The goal is to achieve either the same speeds with lower power output from the propulsion system or higher speeds with the same engine power. This would result in reduced fuel consumption per unit of work performed and, consequently, lower carbon dioxide emissions, improving the ship's energy efficiency.

Reference studies related to air lubrication in the shipping field have primarily focused on ships during the early stages of design. This highlights the significance of the current research, as its main objective is to develop a method of air lubrication that can be applied to ships already in operation, with minimal cost and in a way that sufficiently reduces the vessel's resistance to meeting international energy efficiency standards.

The concept of this research was based on adding side strakes to the bottom of the ship's parallel body, with the aim of creating an external cavity in which air could be injected. Initially, simulations were conducted for the ship alone, without air lubrication, but the effect of the side strakes on increasing resistance were also assessed.

The primary goal of adding side strakes is to form an external cavity on existing ships, in order to maintain and sustain the air layer for as long as possible, as it is not feasible to construct an internal cavity within the hull of ships already in service. This type of modification is typically implemented during the design phase of newly built vessels.

Geometry of the Side Strakes Under the Ship

Fig. 11 shows the initially added side strakes, which consisted of two parallel lines located on the bottom of the parallel midbody section. It is important to note that two different heights for the strakes were used: the first was at 0.25 cm on the model and the second was at 1.25 cm.

Fig. 11. Parallel side strakes added below and on the edges of the parallel part

In the next step, the air injector was added to the beginning and middle of the side strakes, see Fig. 12.

Fig. 12. Air injector position

The injector was designed in the shape of a half-cylinder, to ensure maximum streamlining. This half-cylinder (radius=0.25 cm in the model) was divided into two parts: the front part (shown in green in Fig. 13), acted as a flow deflector, while the rear part (shown in blue) was the section through which air was injected.

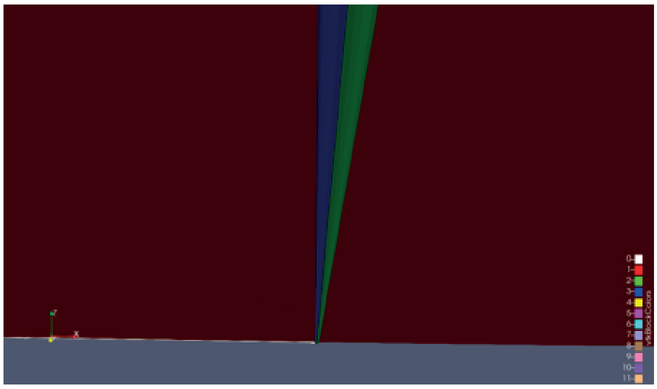

Fig. 13. Position of the air injector

First, the resistance calculations were performed for the two side strakes (two heights) with and without the injector body, to calculate the effect of the injector body on the resistance.

In the third step of the resistance calculation, the strakes were made into a ⊐ shape without the injector, creating a cavity for collecting air, as shown in Fig. 14. The injector was then added, forming a closed rectangle, as shown in Fig. 15. First of all, the calculations were performed without air injection, to determine the effect of these additional structures on the ship's resistance before injecting air.

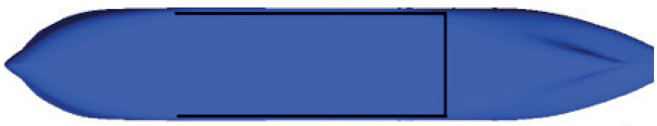

Fig. 14. Side strakes with ⊐ shape

Fig. 15. Side strakes with ⊐ shape with injector

For all calculation cases, structured meshes were generated using the ICEM software. Given that the dimensions of both the strakes and the air injector were very small, compared to the overall size of the ship, a higher mesh density was required to ensure proper coverage, especially on the surfaces of the strakes and injector, as shown in Fig. 16. For this reason, approximately 12 million computational cells were used in cases that included the strakes and the injector.

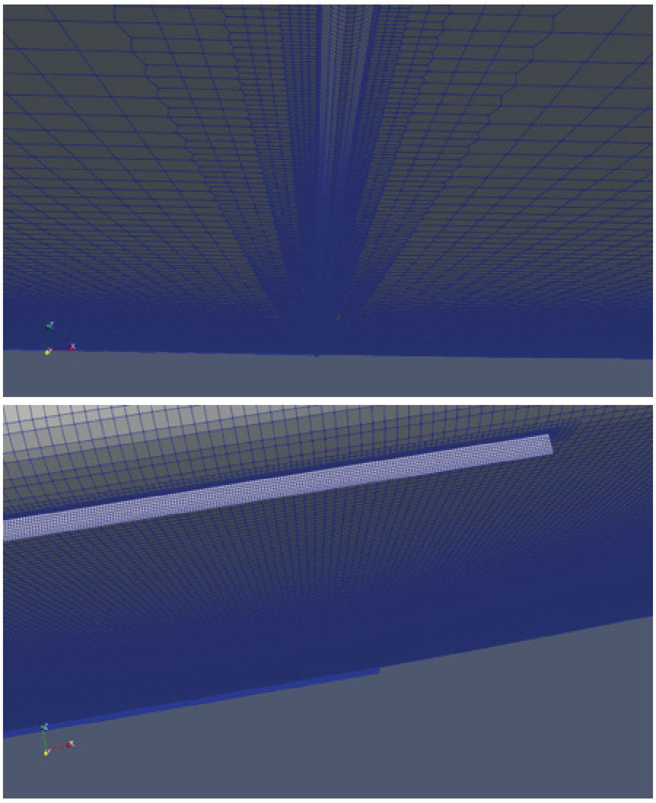

Fig. 16. Mesh refinement on both the injector and the side strakes

Studied Cases

Several cases of the ship were studied, both with and without the strakes, as well as with and without the air injector. Table 10 presents the cases that were analysed for comparison purposes later on.

Tab. 10. Studied cases

Case Number	Case Description
Case 1	Ship without any additions.
Case 2	Ship with parallel side strakes of 0.25 cm height, as shown in Fig. 11.
Case 3	Ship with parallel strakes of 1.25 cm height, as shown in Fig. 11.
Case 4	Ship with ⊃-shaped strakes of 0.25 cm height, as shown in Fig. 14.
Case 5	Ship with ⊃-shaped strakes of 1.25 cm height, as shown in Fig. 14.
Case 6	Ship with parallel strakes of 0.25 cm height, equipped with an air injector at the beginning and middle of the strakes, **without** air injection, as shown in Fig. 12.
Case 7	Ship with parallel strakes of 1.25 cm height, equipped with an air injector at the beginning and middle of the strakes, **without** air injection, as shown in Fig. 12.
Case 8	Ship with ⊃-shaped strakes of 0.25 cm height, equipped with an air injector at the beginning and middle of the strakes, **without** air injection, as shown in Fig. 15.
Case 9	Ship with ⊃-shaped strakes of 1.25 cm height, equipped with an air injector at the beginning and middle of the strakes, **without** air injection, as shown in Fig. 15.
Case 10	Ship with parallel strakes of 0.25 cm height, equipped with an air injector at the beginning and middle of the strakes, as shown in Fig. 12, **with** air injection activated.
Case 11	Ship with parallel strakes of 1.25 cm height, equipped with an air injector at the beginning and middle of the strakes, as shown in Fig. 12, **with** air injection activated.

RESULTS AND DISCUSSION

Before analysing the effect of air injection on reducing the ship's resistance, the impact of adding side strakes in all the cases listed in Table 10 will first be examined, in terms of how much they increase the ship's resistance. This step is essential if we are to exclude configurations that cause a significant increase in resistance.

STUDY OF THE EFFECT OF SIDE STRAKES AND THE INJECTOR BODY ON SHIP RESISTANCE

Initially, it was necessary to calculate the ship's resistance for all the cases listed in Table 10, in order to assess the impact of these additions on overall resistance. If any of the additions cause a significant increase in resistance, their design must be modified before proceeding with air lubrication.

The analysis in all cases was conducted at a speed of 1.179 m/s, which corresponds to a Froude number of 0.142. This Froude number is the same as the Froude number corresponding to the actual service speed of the ship, which is the typical operating speed during most of its voyage.

Tab. 11. Ship resistance in all studied cases

Case No.	R_T[N]	Difference%
Case 1	35.800	[-]
Case 2	35.800	00.000%
Case 3	35.810	00.023%
Case 4	36.000	00.530%
Case 5	41.500	15.920%
Case 6	35.805	00.014%
Case 7	35.820	00.055%
Case 8	36.100	00.834%
Case 9	41.605	16.210%

As shown in Table 11 and illustrated in Fig. 11, the presence of parallel strakes, with heights of 0.25 and 1.25 cm (Case 2 and Case 3), has almost no effect on the ship's total resistance. The primary reason is that these strakes are relatively thin (0.035 cm in the model) and are aligned with the flow direction. As a result, the cross-sectional area facing the flow is only 0.025 cm² for the 0.25 cm strakes and 0.125 cm² for the 1.25 cm strakes (based on the model). These factors collectively explain why adding parallel strakes along the bottom and sides of the midship section does not lead to an increase in resistance.

As also shown in Table 11, the strakes with a height of 0.25 cm cause no notable increase in resistance, while the 1.25 cm strakes lead to only a 0.023% increase, which is negligible.

Turning to the cases that include the injector body but without air injection (Case 6 and Case 7), it was also found that adding the injector body alone results in a slight resistance increase of 0.014% for the 0.25 cm strakes and 0.055% for the 1.25 cm strakes. In both cases, these increases are minimal and can be disregarded. The main reason for the injector's minimal impact is its streamlined shape (a half-cylinder) with a small radius (0.25 cm on the model), as well as its placement at the lower front of the midship section. In this area, the boundary layer is still in the early stages of development and the flow remains laminar, which helps reduce the injector's influence on drag. It should be noted that the injector's streamlined geometry helps prevent the formation of a vortex behind it.

In the cases where ⊐-shaped strakes were added (Case 4 and Case 5), the transverse orientation of these strakes at the end of the midship section led to a noticeable increase in resistance, especially with the 1.25 cm height. Table 11 shows that the 0.25 cm ⊐-shaped strakes (Case 4) caused a resistance increase of 0.53%, whereas the 1.25 cm version (Case 5) resulted in a 15.92% increase. This significant rise is due to the strakes obstructing the flow, causing boundary layer separation and vortex formation (Fig. 17), which significantly increases the ship's drag resistance. The increase caused by the 0.25 cm ⊐-shaped strakes (Case 4) is minor and considered acceptable. However, the increase in Case 5 is substantial and unacceptable, especially since the presence of the injector further raises the resistance to 16.21% in Case 9. In contrast, in Case 8, the presence of the injector, along with 0.25 cm ⊐-shaped strakes, only raises resistance by 0.834%.

Based on the results in Table 11, the following conclusions can be drawn:

– Parallel side strakes, regardless of the studied height (0.25 cm or 1.25 cm), do not have a significant negative impact on drag resistance;
– Including the injector body along with the parallel side strakes does not negatively affect resistance. Thus, parallel side strakes (longitudinally oriented) are preferable for air injection. The optimal height will depend on how well the air layer is sustained beneath the hull, as lower strakes may allow air leakage, which can be prevented with taller strakes;
– Using ⊐-shaped strakes with a height of 0.25 cm does not significantly increase resistance, even with the injector body present. If these strakes succeed in maintaining the air layer beneath the hull, they would be the best option, as they effectively create an external cavity on an existing ship, for continuous air injection;
– ⊐-shaped strakes with a height of 1.25 cm cause a substantial increase in resistance and are, therefore, not a viable option. In this case, the benefits of air injection would be largely offset by the added drag.

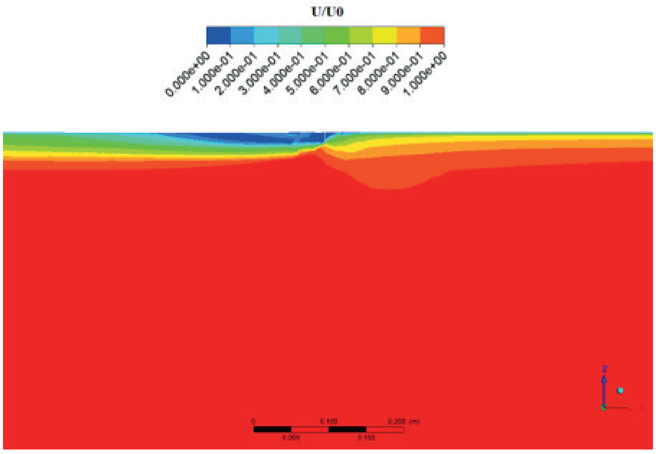

Fig. 17. Boundary layer separation caused by the ⊐-shaped strakes with a height of 1.25 cm

THE EFFECT OF AIR INJECTION ON SHIP RESISTANCE

The following steps were applied:

– Air injection was first applied to both Case 10 and Case 11, as illustrated in Table 10, which involved parallel side strakes with the injector located at the beginning and middle of the strakes;
– If no air leakage occurred in the 0.25 cm high strakes (Case 10), then Case 8 was analysed with air injection included.

Table 12 presents the effect of air injection on ship resistance for both Case 10 and Case 11, which involved parallel side strakes with air injection. As shown in the table, the presence of air lubrication reduces the ship's resistance compared to the same configurations without air injection. However, it is clear that, with 0.25 cm high strakes, the reduction in resistance is only 6.73%. In contrast, when using 1.25 cm high strakes, the resistance decreases by 31.59%, which is a significant improvement. This notable reduction contributes to a substantial increase in the ship's speed for the same engine power, ultimately leading to reduced air pollution caused by the ship.

Tab. 12. Effect of air injection on the ship resistance

Case No.	R_T[N]	Difference%
Case 1	35.80	[-]
Case 10	33.39	-6.73 %
Case 11	24.49	-31.59%

The main reason why resistance is reduced by only 6.73% in Case 10 is that the height of the strakes is insufficient to retain the air layer beneath the ship. This results in significant air leakage from the bottom of the hull, thereby reducing the effectiveness of air lubrication, see Fig. 18. As shown in the figure, air escapes from the beginning of the strakes, which prevents the formation of a continuous air layer under the ship and leads to a loss in the efficiency of the air lubrication system.

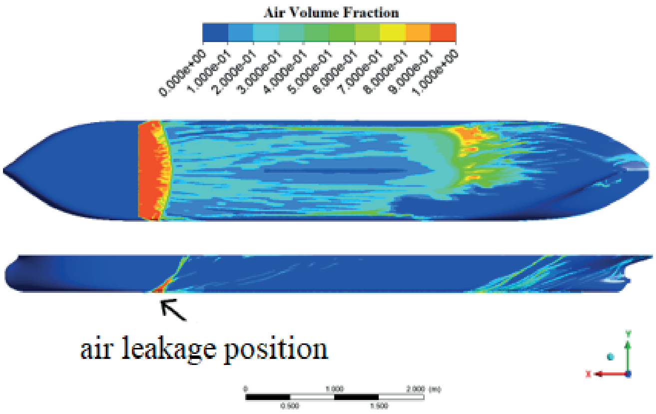

Fig. 18. Air leakage at the beginning of the 0.25 cm high strakes

In the case of the 1.25 cm high strakes, it is observed that the air accumulates properly beneath the strakes, forming an air layer along the lower surface of the parallel midbody section of the hull. This results in a reduction in the ship's drag resistance by approximately 31.59%, see Fig. 19.

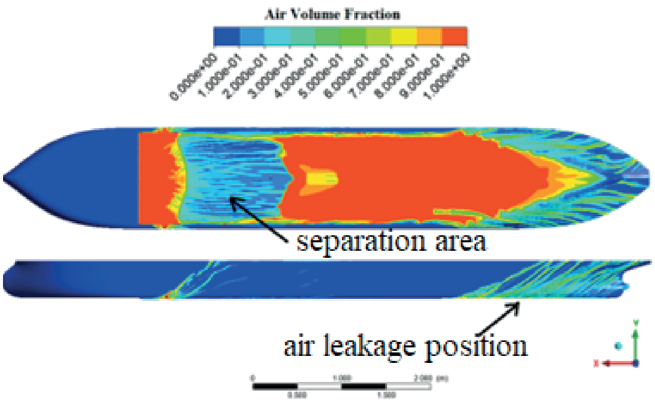

Fig. 19. Formation of an air layer beneath the parallel mid-body section between the strakes (with a height of 1.25 cm), with the primary air leakage occurring at their end

From Fig. 19, we still observe slight air leakage at the beginning of the strakes but it is less, compared to the case with 0.25 cm high strakes. It is also noticeable that the primary leakage occurs after the strakes, along both sides of the ship's stern.

It is well known that air is hydrophobic, which means it resists mixing with water. Therefore, its presence significantly reduces the frictional stresses between the hull and the water, leading to a considerable decrease in resistance. Fig. 20 illustrates the substantial reduction in frictional stress along the lower part of the parallel mid-body section of the hull.

Based on these findings, the 0.25 cm high strakes are not effective for air lubrication and so there was no need to proceed with evaluating the ⊃-shaped strakes under air lubrication conditions.

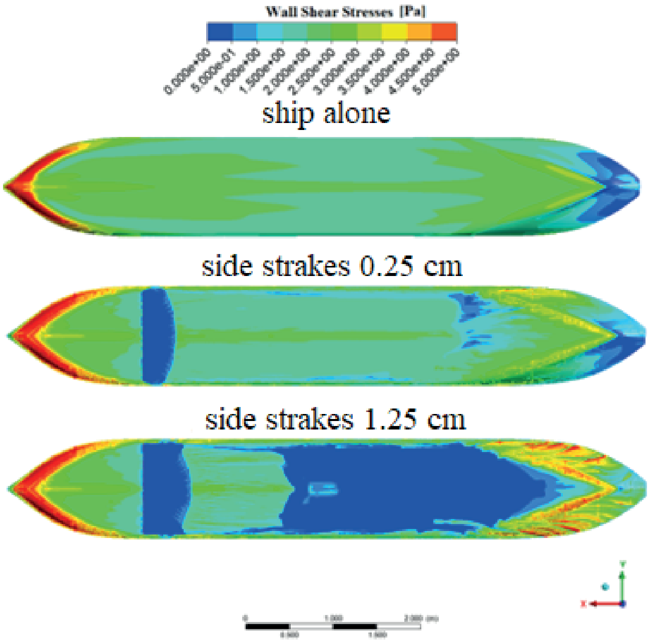

Fig. 20. Reduction of wall shear stresses on the bottom of the parallel mid-body section due to air lubrication

In order to prevent complete air leakage from the first section of the strakes in Case 11, the height of the strakes was increased to 2.5 cm in that section; they were slightly extended to just before the injector, as shown in Fig. 21.

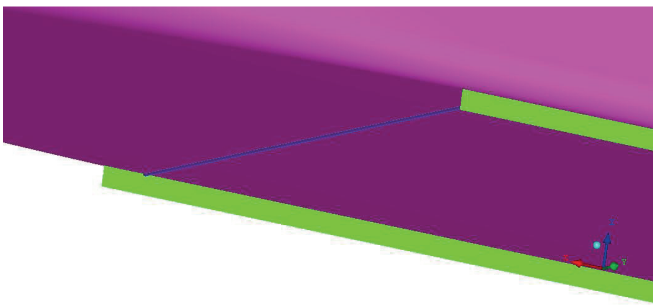

Fig. 21. Increasing the height of the strakes in their front section and extending them slightly before the injector (the injector is shown in blue)

Subsequently, the calculations were repeated for Case 11 and an improvement in resistance reduction was observed, with resistance decreasing by 33.46% compared to the case of the ship without any modifications. It was also noted that there was no air leakage in the first section of the strakes, as shown in Fig. 22. Therefore, this case (Case 11) was adopted for all subsequent calculations in our study.

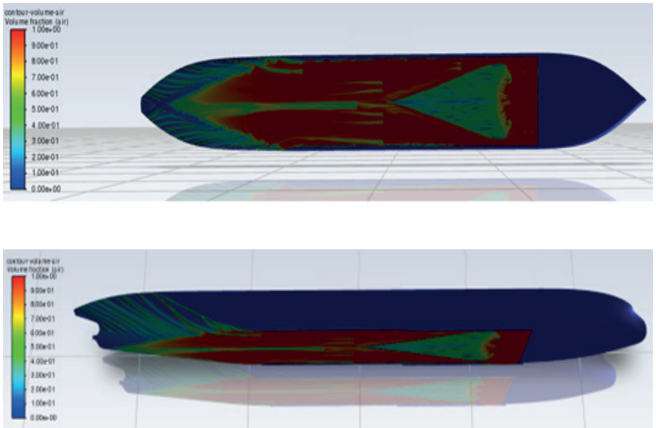

Fig. 22. No air leakage from the beginning of the strakes after increasing their height

STUDY OF THE EFFECT OF VARYING INJECTION SPEED ON AIR LAYER SEPARATION

The air injection speed used in all cases was $1\frac{m}{s}$. Before analysing the impact of air injection on the ship's energy efficiency with the propeller in operation, it was essential to first determine the optimal injection speed that ensured the best distribution of the air layer beneath the ship. For this purpose, several injection speeds (different air flow rates) were tested in Case 4, which involved an increased strake height at the front section. Five injection speeds were examined: 0.100, 0.500, 0.750, 1.000, and 1.179 m/s, noting that the ship's speed was 1.179 m/s. Table 13 illustrates the volumetric air flow rate $Q\ [\frac{L}{s}]$ at each air injection speed $V\ [\frac{m}{s}]$.

Tab. 13. Volumetric air flow rate at each injection speed

$V\ [\frac{m}{s}]$	$Q\ [\frac{L}{s}]$
0.100	0.2500
0.500	1.2500
0.750	1.8750
1.000	2.5000
1.179	2.9475

Based on the results obtained (see Fig. 23), it was observed that, at lower injection speeds (0.10, 0.50, and 0.75 m/s), the air layer experienced separation along the entire middle section of the bottom of the ship's mid-body. At an injection speed of 1.0 m/s, $2.5\frac{L}{s}$ of air, the air layer distribution beneath the hull was found to be very good. Although a separation zone still exists, most of the bottom surface is covered with air.

At an injection speed equal to the ship's speed $(1.179\frac{m}{s})$, which is equal to the ship velocity, mixing of air and water particles exists at the bottom of the ship, leading to distortions in the air layer. This effect was observed in the numerical simulations, as shown in the lower image of Fig. 23.

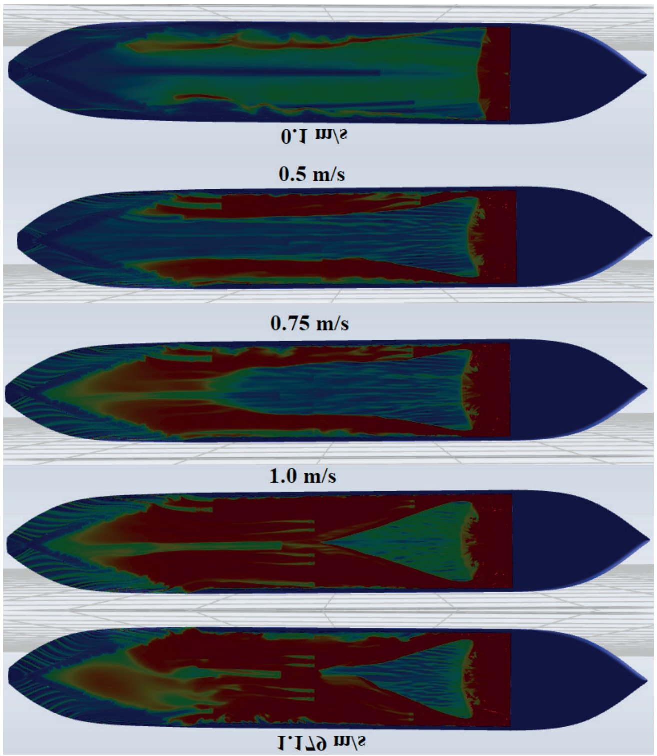

Fig. 23. Effect of air injection speed on air layer distribution

From these results, we note that the maximum airflow rate used in this study is approximately 3 L/s, with a model length of 7 m. In contrast, in the study by Sorrentino et al. (2025) [54], the length of the model (C1505 model) used was 2.313 m and an airflow rate of up to 20.5 L/s was employed.

It is important to note that the regions at the bottom and middle of the parallel mid-body section, where the air layer is interrupted, are not entirely covered by water. Instead, they are covered by a mixture of air and water. This can be observed by examining the fluid density in these regions, as shown in Fig. 24. From this figure, at an injection speed of 0.1 m/s, the fluid density in that area ranges between 1.225 and 800.000 kg/m^3, indicating a mixture of air and water. At an injection speed of 1 m/s, most of the surface is covered with air at a density of 1.225 kg/m^3, while an air-water mixture covers the separation zone at the beginning of the mid-body section.

This is considered to be a positive aspect, since the mixture generally has a lower density than water alone and, thus, its presence is more favourable and contributes to reducing resistance.

One crucial point to bear in mind is that the propeller had not yet been activated in the simulation. Once the propeller was used, it accelerated the flow at the aft part of the hull, which may have increased the difference between the injection speed and the free-stream water velocity. This could lead to an expansion of the separation zones.

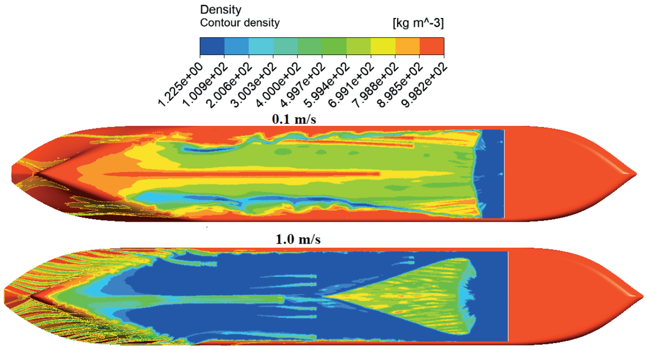

Fig. 24. Density distribution beneath the ship at injection speeds of 0.1 and 1.0 $[\frac{m}{s}]$

AIR LEAKAGE BEFORE REACHING THE PROPELLER

After completing the previous studies, in which the optimal configuration for the side strakes was determined (more specifically, strakes with increased height at the front) and the optimal injection speed was found to be 1 [m/s], it was essential to prevent air from reaching the propeller's operating zone, before proceeding to the calculations stage with the propeller. The presence of air in the propeller region would inevitably lead to a collapse in thrust generation. As a result, the air injection system would shift from being a beneficial solution to having a significantly negative impact.

Accordingly, a V-shaped strake was installed at the end and middle of the existing strakes. It was observed that, with a low height of 0.5 cm, some air leakage into the propeller's operating zone still occurred, as shown in Fig. 25. However, when the strake height was increased to 1.25 cm, it completely prevented air from reaching the propeller region. The presence of this strake did not negatively affect the effectiveness of air lubrication in reducing resistance and successfully fulfilled its purpose of diverting the air before it could reach the propeller's operating area.

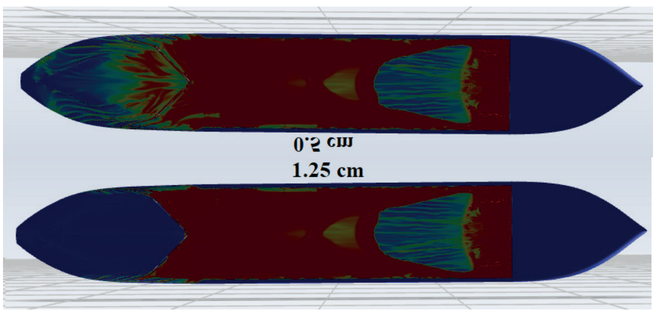

Fig. 25. The role of the V-shaped strake in air diversion

THE EFFECT OF AIR INJECTION ON THE EEXI VALUE OF A SHIP WITH AN OPERATING PROPELLER

At the outset, the CFD results for the ship-propeller system must be validated by comparing them with available experimental data, to verify the quality of the numerical settings and grid. Table 14 shows the percentage error between the numerical and experimental results for ship resistance, propeller thrust, and the torque applied to the propeller in the self-propulsion test, as well as the difference between thrust and resistance for the combined ship-propeller case. All calculations were performed with a Froude number of 0.142, corresponding to a model speed of 1.179 m/s and a propeller speed of 7.8 rps. As seen in the table, the maximum error is −6.77%. Given that wave resistance was neglected in the numerical study, because of the low Froude number, and that experimental results carry an error margin of roughly 1% [34], the numerical results are considered to be good and closely aligned with reality. Consequently, the numerical grid and settings employed here provide reliable results and can be used for subsequent calculations involving the ship and propeller.

Tab. 14. Validation of the numerical results for resistance, thrust, and torque with the propeller

Symbol	$RT_{(with\ propeller)}$ [N]	T[N]	$RT_{(with\ propeller)} - T$	M_z [N.m]
EFD	40.37	22.37	18.00	0.5841
CFD	38.15	21.37	16.78	0.6232
Error%	-6.50%	-4.40%	-6.77%	6.70%

Table 15 presents the resistance and thrust values generated by the MP687 propeller without air injection at a rotational speed of 7.8 rps (which is the speed that was experimentally tested). As shown in the table, the resistance value is greater than the thrust ($R_T > T$) and, therefore, it was necessary to increase the number of revolutions to achieve a balance between resistance and thrust. The number of revolutions was increased to 10 rps. As shown in Table 15, at this rotational speed, the thrust generated by the propeller exceeds the resistance by 1.18%, which is a very small amount $\left(\frac{T-R_T}{R_T} \times 100 = 1.18\%\right)$.

Tab. 15. Resistance and thrust results generated by the MP687 propeller

n rps	R_T [N]	T [N]
7.8	38.15	21.37
10.0	40.45	40.93

Therefore, a rotational speed of 10 rps can be considered to be the appropriate rotational speed, which causes the ship to move at a velocity of 1.179 m/s. At this value, the torque acting on the propeller was 1.136 Nm.

Performing the air injection process with the propeller operating at a speed of 10 rps clearly resulted in a reduction of resistance. The new ship speed with air injection was then searched for, at which the thrust equals the ship's resistance at the same torque delivered to the propeller (which equals) 1.136 [$m \cdot N$]and the same engine power. The new ship speed, with the same power delivered to the propeller, was 1.42 m/s. Therefore, the ship speed increased from 1.179 to 1.420 m/s.

When comparing the two scenarios (both with and without air injection) based on Eq.)8(, while maintaining constant propeller power delivery (implying a constant P_{ME} and constant MCR_{ME}), all other parameters in the EEXI calculation remain unchanged for a given ship. These include:
- Ship capacity (deadweight);
- Fuel-specific emission factors (CF_{ME}, CF_{AE});

–Specific fuel consumption values (SFC_{ME}, SCF_{AE}).

Consequently, Eq.)8(can be simplified to:

$$\mathbf{EEXI_{attained}} = \frac{contant}{\cdot\ V_{ref}} \qquad)14($$

Accordingly, the value of $EEXI_{attained}$ in both cases can be written as follows:

$$\mathbf{EEXI_{att1}} = \frac{contant}{1.179} \qquad)15($$

$$\mathbf{EEXI_{att2}} = \frac{contant}{1.420} \qquad)16($$

Where:

$EEXI_{att1}$: Energy Efficiency Existing Ship Index without air injection (ship speed equals 1.179 m/sec);

$EEXI_{att2}$: Energy Efficiency Existing Ship Index with air injection (ship speed equals 1.420 m/sec).

By taking the percentage difference between the two values, we find $\frac{EEXI_{att2} - EEXI_{att1}}{EEXI_{att1}} \times 100\% = -16.97\%$, meaning that the value of the Energy Efficiency Existing Ship Index decreases by 16.97% when using the air lubrication technology in the presence of the MP687 propeller in working conditions. The lower the index value, the lower the CO_2 emissions, since the unit of the index is [$gr \frac{CO^2}{Ton} \cdot Nm$].

As expected, the presence of the propeller led to an increase in the separation area of the air layer beneath the parallel body section, see Fig. 26. The reason for this is the suction effect of the propeller, which causes an increase in velocity around the ship's hull, especially in the stern area. This leads to a greater difference between the injection speed and the water speed, thus increasing the separation area of the air layer.

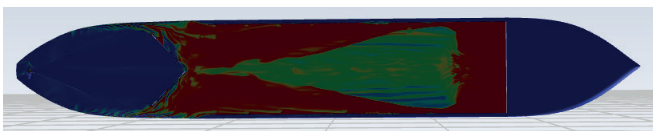

Fig. 26. Separation of the air layer in the presence of the operating propeller

Fig. 27 shows a side view of the stern area, illustrating how the air leaks before reaching the propeller.

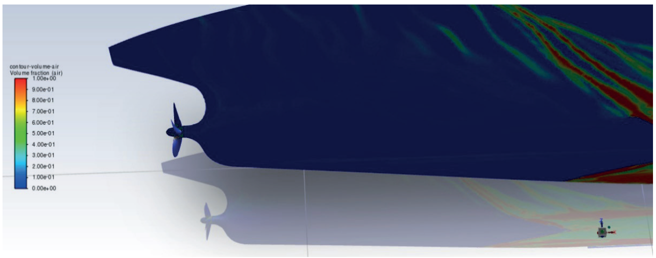

Fig. 27. Air leakage before reaching the propeller

CONCLUSIONS

In this study, a method was proposed to utilise air lubrication technology for ships with a large parallel midbody section that are already in service, in order to comply with the International Maritime Organization (IMO) energy efficiency standards. The proposed approach involves adding side strakes to the sides and bottom of the parallel midbody to create an external cavity capable of trapping air and preventing its leakage. A V-shaped strake was also added to the bottom and aft end of the parallel midbody, to release the air before it reaches the propeller, as the presence of air at the propeller has a significantly negative effect on its performance and efficiency.

Based on this work, the following conclusions were drawn:
- Air lubrication plays a significant positive role in reducing ship resistance.
- The implementation of air lubrication technology reduced total ship resistance, resulting in a 16.67% improvement in the attained EEXI value. This reduction directly correlates with lower CO_2 emissions per unit of transport work (measured in grams of CO_2 per ton x nautical miles), demonstrating the system's potential to enhance compliance with IMO's carbon intensity regulations without compromising operational performance.
- **The improvement value of 16.67% was obtained with the model at a 1:40 scale, while neglecting the effects of both waves and ship motions (heave, pitch, roll, etc.). Accordingly, in the case of a real ship operating under actual sea conditions, this value will, of course, be less than 16.67%.**
- The height of the side strake is critical for maintaining the air layer beneath the ship. A height of 0.25 cm is insufficient for the bulk carrier model.
- The height of 1.25 cm for the side strakes is suitable for maintaining the air layer beneath the ship model.
- The proposed method can be applied to any bulk carrier or oil tanker currently in service, as these types of ships have large parallel midbody sections.
- Increasing the height of the strakes at their initial sections effectively prevents air leakage.

– The air injection speed (i.e. the flow rate of injected air) significantly affects the distribution and continuity of the air layer beneath the ship.
– Implementing air injection contributes significantly to improving the ship's energy efficiency at minimal cost.
– Releasing air before it reaches the propeller is very important, as the arrival of air at the operating propeller causes a collapse in the generated thrust.
– The proposed method is feasible for application to any bulk carrier or oil tanker in service, given their large parallel body sections.

REFERENCES

1. Kanifolskyi O, "General Strength, Energy Efficiency (EEDI), and Energy Wave Criterion (EWC) of Deadrise Hulls for Transitional Mode," Polish Marit. Res., vol. 29, no. 3, pp. 4–10, Sep. 2022, doi: 10.2478/POMR-2022-0021.

2. Mindykowski J, Wierzbicki Ł, Górniak M, Piłat A, "Analysis and Experimental Verification of Improving the EEDI of a Ship using a Thruster Supplied by a Hybrid Power System," Polish Marit. Res., vol. 31, no. 1, pp. 43–54, Mar. 2024, doi: 10.2478/POMR-2024-0005.

3. Ammar NR, Almas M, Nahas Q, "Economic Analysis and the EEXI Reduction Potential of Parallel Hybrid Dual-Fuel Engine Fuel Cell Propulsion Systems for LNG Carriers," Polish Marit. Res., vol. 30, no. 3, pp. 59–70, Sep. 2023, doi: 10.2478/POMR-2023-0039.

4. IMO, "Resolution MEPC.212 (63)-Guidelines on the Method of Calculation of the Attained Energy Efficiency Design Index (EEDI) for New Ships," IMO, London, UK., 2012, [Online]. Available: https://wwwcdn.imo.org/localresources/en/KnowledgeCentre/IndexofIMOResolutions/MEPCDocuments/MEPC.212(63).pdf.

5. IMO, "Resolution MEPC.336 (76)-Guidelines on Operational Carbon Intensity Indicators and the Calculation Methods (CII Guidelines, G1)," IMO, London, UK., 2021, [Online]. Available: https://wwwcdn.imo.org/localresources/en/OurWork/Environment/Documents/Air pollution/MEPC.336(76).pdf.

6. IMO, "Resolution MEPC.337 (76)-Guidelines on the Reference Lines for Use with Operational Carbon Intensity Indicators (CII Reference Lines Guidelines, G2).," IMO, London, UK., 2021, [Online]. Available: https://wwwcdn.imo.org/localresources/en/OurWork/Environment/Documents/Air pollution/MEPC.337(76).pdf.

7. Sinay, "Eco-Friendly Shipping: Transforming Maritime Sustainability." https://sinay.ai/en/eco-friendly-shipping-transforming-maritime-sustainability/ (accessed Jun. 28, 2025).

8. IMO, "IMO's work to cut GHG emissions from ships." https://www.imo.org/en/MediaCentre/HotTopics/Pages/Cutting-GHG-emissions.aspx (accessed Jun. 28, 2025).

9. IMO, "Improving the energy efficiency of ships." https://www.imo.org/en/OurWork/Environment/Pages/Improving the energy efficiency of ships.aspx (accessed Jun. 28, 2025).

10. Zhang D, Li Y, Gong J, "Study on the Effect of Air Injection Location on the Drag Reduction in SWATH with Air Lubrication," J. Mar. Sci. Eng. Vol. 11, Page 667, vol. 11, no. 3, p. 667, Mar. 2023, doi: 10.3390/JMSE11030667.

11. Madavan NK, Deutsch S, Merkle CL, "Reduction of turbulent skin friction by microbubbles," Phys. Fluids, vol. 27, no. 2, pp. 356–363, Feb. 1984, doi: 10.1063/1.864620.

12. Mäkiharju SA, Perlin M, Ceccio SL, "On the energy economics of air lubrication drag reduction," Int. J. Nav. Archit. Ocean Eng., vol. 4, no. 4, 2012, doi: 10.3744/jnaoe.2012.4.4.412.

13. Ceccio SL, "Friction drag reduction of external flows with bubble and gas injection," Annual Review of Fluid Mechanics, vol. 42. 2010, doi: 10.1146/annurev-fluid-121108-145504.

14. Mizokami S, Kuroiwa R, "Installation of Air Lubrication System for Ro-Pax Ferry and Verification of its Effect in Actual Seas Based on Onboard Measurement Data," J. Japan Soc. Nav. Archit. Ocean Eng., vol. 29, no. 0, pp. 1–9, 2019, doi: 10.2534/JJASNAOE.29.1,.

15. Ship Universe, "Hull Optimization Strategies in 2025: What's Hot and What's Cold? – Ship Universe." https://www.shipuniverse.com/hull-optimization-strategies-in-2025-whats-hot-and-whats-cold/ (accessed Jun. 28, 2025).

16. Mitsubishi Heavy Industries, "MHI Installs MALS (Mitsubishi Air Lubrication System) on a Ferry For First Time and Verifies Over 5% Fuel Efficiency Improvement-Sights On Expanded System Applications to High-speed, Slender Hull-form Ships - Mitsubishi Heavy Industries." https://www.mhi.com/news/1210031580.html (accessed Jun. 29, 2025).

17. Jang J, Choi SH, Ahn SM, Kim B, Seo JS, "Experimental investigation of frictional resistance reduction with air layer on the hull bottom of a ship," Int. J. Nav. Archit. Ocean Eng., vol. 6, no. 2, 2014, doi: 10.2478/IJNAOE-2013-0185.

18. Freitas FR, Moraes DEB, Warkentin S, Mais LA, Ivers JF, Taddei JAAC, "Maternal restrictive feeding practices for child weight control and associated characteristics," Jornal

de Pediatria (Versão em Português)., vol. 95, no. 2, pp. 201–208, Mar. 2019, doi: 10.1016/J.JPED.2017.12.009.

19. Pavlov GA, Yun L, Bliault A, He SL, “Air lubricated and air cavity ships: Development, design, and application,” Air Lubr. Air Cavity Ships Dev. Des. Appl., pp. 1–469, Jan. 2020, doi: 10.1007/978-1-0716-0425-0/COVER.

20. Silberschmidt N, Tasker D, Pappas T, Johannesson J, “Silverstream® System – Air Lubrication Performance Verification and Design Development,” 10th Symp. High-Performance Mar. Veh., pp. 236–246, 2016, [Online]. Available: https://conferences.ncl.ac.uk/media/sites/conferencewebsites/scc2016/1.3.2.pdf.

21. Armada Technologies, “Home - Armada Technologies.” https://armada-technologies.com/ (accessed Jul. 11, 2025).

22. Alfa Laval, “OceanGlide- Air lubrication system, Alfa Laval.” https://www.alfalaval.com/products/process-solutions/fluidic-air-lubrication/oceanglide/ (accessed Jul. 11, 2025).

23. Menter FR, “Two-equation eddy-viscosity turbulence models for engineering applications,” AIAA J., vol. 32, no. 8, pp. 1598–1605, Aug. 1994, doi: 10.2514/3.12149.

24. Abbas N, Kornev N, Shevchuk I, Anschau P, “CFD prediction of unsteady forces on marine propellers caused by the wake nonuniformity and nonstationarity,” Ocean Eng., 2015, doi: 10.1016/j.oceaneng.2015.06.007.

25. Abbas N, Kornev N, “Study of unsteady loadings on the propeller under steady drift and yaw motion using URANS, hybrid (URANS-LES) and LES methods,” Sh. Technol. Res., vol. 63, no. 2, pp. 121–131, May 2016, doi: 10.1080/09377255.2016.1211582.

26. Kornev N, Abbas N, “Numerical Simulation of the tip vortex behind a wing oscillated with a small amplitude,” J. Aircr., vol. 54, no. 2, 2017, doi: 10.2514/1.C033945.

27. Abbas N, Kornev N, “Validation of hybrid URANS/LES methods for determination of forces and wake parameters of KVLCC2 tanker at manoeuvring conditions,” Sh. Technol. Res., vol. 63, no. 2, pp. 96–109, May 2016, doi: 10.1080/09377255.2016.1157275.

28. Abbas N, Barbahan M, Kabrial Y, Kabrial A, “A Novel Approach to Wave Energy Conversion Using CFD Technique,” Polish Marit. Res., vol. 31, no. 3, pp. 113–125, Sep. 2024, doi: 10.2478/POMR-2024-0041.

29. Hirt CW, Nichols BD, “Volume of fluid (VOF) method for the dynamics of free boundaries,” J. Comput. Phys., vol. 39, no. 1, pp. 201–225, Jan. 1981, doi: 10.1016/0021-9991(81)90145-5.

30. Wei Song K, Yu Guo C, Wang C, Sun C, Li P, Fan Zhong R, “Experimental and numerical study on the scale effect of stern flap on ship resistance and flow field,” Ships Offshore Struct., vol. 15, no. 9, 2019, doi: 10.1080/17445302.2019.1697091.

31. Lee H, Rhee SH, “A dynamic interface compression method for VOF simulations of high-speed planing watercraft,” J. Mech. Sci. Technol., vol. 29, no. 5, pp. 1849–1857, May 2015, doi: 10.1007/S12206-015-0405-6/METRICS.

32. Queutey P, Visonneau M, “An interface capturing method for free-surface hydrodynamic flows,” Comput. Fluids, vol. 36, no. 9, pp. 1481–1510, Nov. 2007, doi: 10.1016/J.COMPFLUID.2006.11.007.

33. Rhee SH, Makarov BP, Krishinan H, Ivanov V, “Assessment of the volume of fluid method for free-surface wave flow,” J. Mar. Sci. Technol., vol. 10, no. 4, pp. 173–180, Dec. 2005, doi: 10.1007/S00773-005-0205-2/METRICS.

34. Tokyo 2015, “A Workshop on CFD in Ship Hydrodynamics.” Accessed: 28-Jun-2023. [Online]. Available: https://t2015.nmri.go.jp/jbc.html.

35. Hino T, Stern F, Larsson L, Visonneau M, Hirata N, Kim J, “Numerical Ship Hydrodynamics: An Assessment of the Tokyo 2015 Workshop,” Tokyo 2015, vol. 94, 2021, doi: 10.1007/978-3-030-47572-7.

36. Tokyo 2015, “T2015 - jbc_Geometry.” https://www.t2015.nmri.go.jp/jbc_gc.html (accessed Nov. 10, 2024).

37. Tokyo 2015, “Open Water Tests for JBC (NMRI) MODEL PROPELLER NO.687.” 2015, Accessed: 28-Jun-2025. [Online]. Available: https://www.t2015.nmri.go.jp/Instructions_JBC/instruction_JBC_files/Open_Water_Tests_for_JBC_NMRI.txt.

38. ITTC, “International Towing Tank Conference. Recommended Procedures and Guidelines 7.5-03-02-03, Practical Guidelines for Ship CFD Applications,” 26th International Towing Tank Conference. 2011, [Online]. Available: http://ittc.info/media/1357/75-03-02-03.pdf.

39. ITTC, “International Towing Tank Conference. Recommended Procedures and Guidelines 7.5-03-02-03, Practical Guidelines for Ship CFD Applications,” 27th International Towing Tank Conference. 2014, [Online]. Available: https://www.ittc.info/media/8165/75-03-02-03.pdf.

40. Marine Environmental Protection Committee, “Mepc.350(78) - Guidelines On The Method Of Calculation Of The Attained Energy Efficiency Existing Ship Index (EEXI),” IMO Publ., vol. 304, no. June, pp. 1–11, 2022, [Online]. Available: https://

wwwcdn.imo.org/localresources/en/KnowledgeCentre/IndexofIMOResolutions/MEPCDocuments/MEPC.350(78).pdf.

41. IMO, "Resolution MEPC.308 (73)-Guidelines on the method of calculation of the attained energy efficiency design index (EEDI) for new ships," IMO, London, UK., 2018, [Online]. Available: https://wwwcdn.imo.org/localresources/en/OurWork/Environment/Documents/Air pollution/MEPC.308(73).pdf.

42. International Maritime Organization (IMO), "MARPOL - International Convention for the Prevention of Pollution from Ships - Annex VI - Regulations for the Prevention of Air Pollution from Ships - Chapter 4 - Regulations on Energy Efficiency for Ships - Regulation 25 - Required EEXI," vol. 44, no. October, 2025, [Online]. Available: https://wwwcdn.imo.org/localresources/en/MediaCentre/HotTopics/Documents/Circular Letter No.5005 - Draft Revised Marpol Annex Vi (Secretariat).pdf.

43. International Maritime Organization (IMO), "MARPOL - International Convention for the Prevention of Pollution from Ships - Annex VI - Regulations for the Prevention of Air Pollution from Ships - Chapter 4 - Regulations on Energy Efficiency for Ships - Regulation 24 - Required EEDI," vol. 44, no. October, 2025, [Online]. Available: https://wwwcdn.imo.org/localresources/en/MediaCentre/HotTopics/Documents/Circular Letter No.5005 - Draft Revised Marpol Annex Vi (Secretariat).pdf.

44. Stern F, Wilson RV, Coleman HW, Paterson EG, "Verification and validation of CFD simulations," Proc. 1999 3rd ASME/JSME Jt. Fluids Eng. Conf. FEDSM'99, San Fr. California, USA, 18-23 July 1999.

45. Stern F, Wilson RV, Coleman HW, Paterson EG, "Comprehensive approach to verification and validation of CFD simulations—Part 1: Methodology and procedures," J. Fluids Eng. Trans. ASME, vol. 123, no. 4, 2001, doi: 10.1115/1.1412235.

46. Wilson RV, Stern F, Coleman HW, Paterson EG, "Comprehensive approach to verification and validation of CFD simulations—Part 2: Application for rans simulation of a cargo/container ship," J. Fluids Eng. Trans. ASME, vol. 123, no. 4, 2001, doi: 10.1115/1.1412236.

47. Stern F, Wilson R, Shao J, "Quantitative V&V of CFD simulations and certification of CFD codes," Int. J. Numer. Methods Fluids, vol. 50, no. 11, pp. 1335–1355, Apr. 2006, doi: 10.1002/FLD.1090.

48. ITTC, "Uncertainty Analysis in CFD Verification and Validation Methodology and Procedures," 25th International Towing Tank Conference. pp. 1–12, 2008, [Online]. Available: https://www.ittc.info/media/8153/75-03-01-01.pdf.

49. Xing T, Stern F, "Factors of safety for Richardson extrapolation," J. Fluids Eng. Trans. ASME, vol. 132, no. 6, pp. 614031–640313, Jun. 2010, doi: 10.1115/1.4001771/456309.

50. Mohamed Sukri Mat ALI CJD, Wheatley V, "Grid convergence study for a two-dimensional simulation of flow around a square cylinder at a low Reynolds number," in Seventh International Conference on CFD in the Minerals and Process Industries, CSIRO, Melbourne, Australia, [Online]. Available: https://flair.monash.edu/intranet/proceedings/cfd2009/PDFs/136ALI.pdf.

51. Koo B, Yang J, Yeon SM, Stern F, "Reynolds and froude number effect on the flow past an interface-piercing circular cylinder," Int. J. Nav. Archit. Ocean Eng., vol. 6, no. 3, pp. 529–561, Sep. 2014, doi: 10.2478/IJNAOE-2013-0197.

52. Tokyo 2015, "JBC-Case 1.3a," 2015. https://www.t2015.nmri.go.jp/Instructions_JBC/Case_1-3a.html (accessed Nov. 03, 2024).

53. Tokyo 2015, "JBC Case 1.5a," 2015. https://www.t2015.nmri.go.jp/Instructions_JBC/Case_1-5a.html (accessed Jul. 19, 2024).

54. Sorrentino V, Pigazzini R, De Luca F, Mancini S, Pensa C, "Experimental and numerical investigation of air lubrication on a planing hull with Double Interceptor System," Ocean Eng., vol. 319, p. 120135, Mar. 2025, doi: 10.1016/J.OCEANENG.2024.120135.